metals

MDPI

*Article*

# Effect of Annealing Temperature on Recrystallization Behavior of 0.25 mm Thin-Gauge Non-Oriented Electrical Steel

**Xiaoyu Lu [1], Xiaoming Yuan [1,*], Rong Chai [2], Lifeng Fan [2] and Lili Dong [3]**

[1] Inner Mongolia Baotou Steel Union Co., Ltd., Baotou 014010, China
[2] School of Materials Science and Engineering, Inner Mongolia University of Technology, Hohhot 010051, China
[3] School of Materials Science and Engineering, Baotou Iron and Steel Vocational Technical College, Baotou 014010, China
* Correspondence: 18648613656@163.com

**Abstract**

Aiming at the performance regulation demand for high-grade thin-gauge non-oriented electrical steel, 0.25 mm thick non-oriented electrical steel containing 3.53 wt.% Si was taken as the research object to investigate the effects of annealing temperature ranging from 850 °C to 1000 °C on its microstructure, texture characteristics, precipitates and magnetic properties. The results show that with increasing annealing temperature, the recrystallized grain size of the specimen increases first and then decreases, and the average grain size reaches a peak of 161.376 μm at 975 °C. At 950 °C, favorable textures including 4.6% {110}<001> Goss texture and 3.58% {001}<350> texture are formed, yielding the maximum magnetic flux density $B_{50}$ of 1.865 T and a core loss $P_{1.0/400}$ of 10.85 W/kg. The specimen annealed at 950 °C has a coercivity Hc of 62.64 A/m and a remanence Br of 515.2 mT. Overall, annealing at 950 °C achieves the optimal matching of magnetic induction and core loss for this thin-gauge non-oriented electrical steel. The research results can provide theoretical and data support for optimizing the annealing process of high-grade non-oriented electrical steel.

**Keywords:** non-oriented electrical steel; microstructure; texture; magnetic property

## 1. Introduction

Driven by the goals of energy conservation, carbon peaking and carbon neutrality, new energy technologies have developed rapidly, and high-frequency ultra-thin non-oriented electrical steel has gradually become a key research focus [1]. Meanwhile, non-oriented electrical steel is required to have higher magnetic flux density to boost motor torque and enable motor miniaturization, as well as lower core loss to improve motor efficiency [2–7]. Reducing sheet thickness is the most effective approach to reduce core loss and product volume. However, as cold rolling reduction increases, the fraction of γ-fiber texture (<111>//ND or {111}⊥ND) rises gradually, making it difficult to simultaneously achieve high magnetic flux density and low core loss [8]. The microstructure and texture are closely correlated with annealing temperature and final sheet thickness.

Annealing is the final processing step for non-oriented electrical steel. It determines the grain size and texture of the finished product [9], and thus governs the magnetic prop-

Received: 18 October 2026
Revised: 12 November 2026
Accepted: 17 November 2026
Published: 18 November 2026

**Copyright:** © 2026 by the authors. Licensee MDPI, Basel, Switzerland. This article is an open access article distributed under the terms and conditions of the Creative Commons Attribution (CC BY) license.

erties. During annealing, the material undergoes three successive stages: recovery, recrystallization nucleation, and grain growth. Li et al. [10] found that for 3.3% Si–0.9% Al–1.0% Mn non-oriented electrical steel, as annealing temperature increases, the proportion of recrystallized structure rises, the content of deformation-induced {111} texture first decreases then increases, the fraction of favorable {100} and {110} textures grows continuously, and the texture factor first rises then falls; both $P_{1.5/50}$ and $P_{1.0/400}$ decrease significantly, while $B_{50}$ first increases then decreases, reaching a maximum of 1.616 T at 725 °C. Yin et al. [11] used W350 high-grade non-oriented silicon steel, with the annealing temperature and annealing time held constant, and found that as the annealing temperature increased and the holding time was extended, the $\alpha$-fiber texture gradually transformed into an $\alpha*$-fiber texture, while the cubic texture tended to aggregate toward {001}<210>; furthermore, the $\gamma$-fiber texture component and strength decreased markedly. Yu et al. [12] reported that for 2.84% Si–0.2% Ni non-oriented electrical steel, higher annealing temperature strengthens the favorable $\alpha$-fiber texture and weakens the unfavorable $\gamma$-fiber texture, thus reducing core loss; the magnetic flux density first rises then falls, following the same trend as $\alpha$-fiber texture density, and strong $\alpha$-fiber texture is beneficial for improving magnetic flux density. Nevertheless, excessively high annealing temperature leads to oversized grains and unfavorable $\gamma$ texture. Jiao et al. [13] investigated the effect of annealing temperature (900–1200 °C) on the microstructure and texture of non-oriented electrical steel. Below 1100 °C, core loss shows a decreasing trend; when the temperature rises to 1200 °C, core loss increases significantly due to abnormally coarse grains, which is attributed to the fact that $\eta$-fiber texture first strengthens, then weakens, while off-$\gamma$-fiber and $\lambda$-fiber textures strengthen continuously. Therefore, systematic investigation into the comprehensive effect of annealing temperature on the microstructure, texture and magnetic properties of non-oriented electrical steel is essential for further performance improvement.

Total core loss ($P_t$) consists of eddy current loss ($P_e$) and hysteresis loss ($P_h$). According to Maxwell's equations, eddy current loss is proportional to sheet thickness, so thickness reduction can effectively lower core loss. Wang et al. [14] found that for 3.27% Si non-oriented electrical steel, with increasing rolling reduction, the microstructure evolves from grain elongation to shear band formation and finally to fiber structure. At a reduction of 60–70%, the texture transforms from rotated cube and $\alpha$-fiber textures to $\gamma$-fiber and Goss textures. As reduction increases from 84.6% to 88.6%, shear bands in the cold-rolled sheet diminish gradually, and deformed grains evolve into strip-shaped fiber structure along the rolling direction; the dominant texture shifts from {110}<111> in shear bands to {111}<110> and {112}<111> in fiber structure [15].

In summary, reducing the sheet thickness can lower eddy-current losses; however, a high cold rolling reduction rate tends to induce an unfavorable $\gamma$-fiber texture, thereby limiting the simultaneous improvement in magnetic properties. The annealing process alters the texture composition—including $\alpha$, $\alpha^*$, and $\gamma$ phases—as well as the grain size, by controlling the processes of recovery, recrystallization, and grain growth. The recrystallization texture evolution mechanism of non-oriented electrical steel under large rolling reduction, and the regulatory effect of annealing on microstructure and magnetic properties, still require systematic investigation. In this work, 0.25 mm thick 3.5% Si non-oriented electrical steel was used to explore the influence of different annealing temperatures on its microstructure, texture and magnetic properties, and to identify the optimal annealing parameters. The results can provide theoretical and data support for the annealing process optimization of high-grade thin-gauge non-oriented electrical steel.

## 2. Materials and Methods

The raw material was a hot-rolled sheet of 3.53% Si–0.049% Sn non-oriented electrical steel provided by an industrial manufacturer (chemical composition given in Table 1). The finish rolling temperature was 880 °C; then, a two-pass hot rolling test mill was used to carry out five-pass rolling, and the final thickness of the hot-rolled sheet was 2.3 mm. The hot-rolled sheet was first subjected to normalizing treatment at 875 °C for 5 min. The normalized sheet with an initial thickness of 2.3 mm was cold-rolled to 0.25 mm via six passes on a 20-high reversible cold mill. The thickness after each pass was 1.55 mm, 1.08 mm, 0.76 mm, 0.53 mm, 0.36 mm and 0.25 mm, corresponding to a total cold reduction of 89.13%. Isothermal annealing was then performed in a tube annealing furnace at temperatures of 850 °C, 875 °C, 900 °C, 925 °C, 950 °C, 975 °C and 1000 °C for 3 min, with 100% $N_2$ as the protective atmosphere.

**Table 1.** Mass percentage of elements in non-oriented silicon steel (wt.%).

| Element | Si | Als | Mn | P | Ti | C, S, N | Sn |
|---|---|---|---|---|---|---|---|
| | 3.53 | 0.73 | 0.52 | 0.017 | 0.0014 | ≤0.002 | 0.049 |

Specimens from the hot-rolled, normalized and annealed states were mechanically polished and etched with 4 vol.% nital solution for 35–50 s. Microstructure observation and image acquisition were carried out using an Olympus GX51F inverted metallographic microscope (Olympus Corporation, Tokyo, Japan); the grain size of the microstructure obtained after annealing was determined using the cross-sectional method. The specimen was cut along the rolling direction to dimensions of 8 mm × 10 mm; it was then sequentially water-polished with 400#, 800#, 1200#, and 2000# SiC abrasive papers, followed by 2.5 μm diamond polishing. The morphology of precipitates was examined with an FEI QUANTA 650 field emission scanning electron microscope (FE-SEM, FEI Company, Hillsboro, OR, USA). Electron backscatter diffraction (EBSD) data were collected. EBSD characterization was performed on the longitudinal section (RD–ND plane) using a field-emission scanning electron microscope equipped with an EBSD detector. The accelerating voltage was set to 20 kV, the specimen tilt angle was 70°, and the scanning step size was 1.5 μm. The collected data were post-processed with HKL Channel 5 software, and grain boundaries were defined with a misorientation threshold of 15°. Magnetic properties, namely magnetic flux density B50 and core loss $P_{1.0/400}$, were measured on 12 mm (RD) × 30 mm(TD) single-sheet specimens using a MATS-3000M silicon steel tester (Hunan Lianzhong Co., Ltd., Hunan, China).

## 3. Results

Figure 1 shows the microstructure, orientation map and micro-texture map of the hot-rolled sheet. As seen in (a), the microstructure exhibits pronounced through-thickness inhomogeneity: the surface layer consists of fine recrystallized grains, the subsurface layer shows a mixture of recrystallized grains and band-shaped deformed structure, and the central layer is dominated by elongated banded deformation structure along the rolling direction [16,17]. Quantitatively (Table 2), the surface texture is dominated by {112}<110> with a volume fraction of 20.9%, followed by {111}<110> at 17.3% and {221}<110> at 11.6%. These three components all belong to $\alpha$-fiber texture (<110>//RD), and their total fraction is close to 50%. In addition, {023}<100> and {001}<350> textures are present as minor components, accounting for 8.05% and 6.62%, respectively.

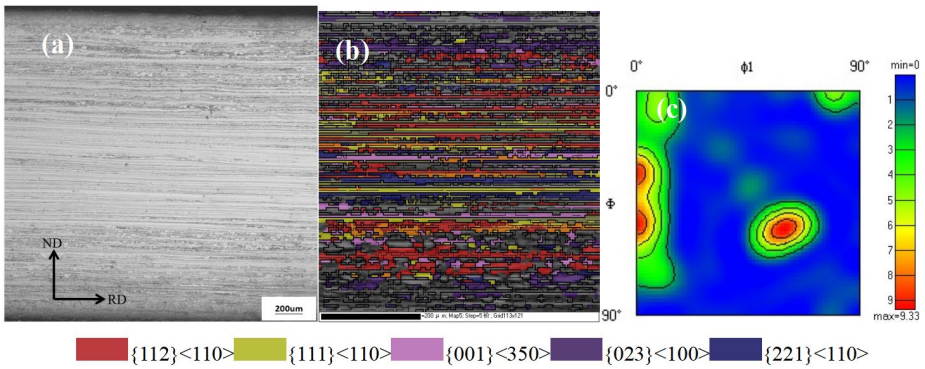


**Figure 1.** Microstructure, grain orientation maps and micro-texture diagrams of hot-rolled steel sheets. (**a**) microstructure; (**b**)orientation map; (**c**)micro-texture diagram.

**Table 2.** Texture content of hot-rolled steel sheets (%).

| {112}<110> | {111}<110> | {001}<350> | {023}<100> | {221}<110> |
|---|---|---|---|---|
| 20.9 | 17.3 | 6.62 | 8.05 | 11.6 |

Figure 2 presents the SEM morphology and EDS spectra of precipitates in the hot-rolled sheet, with corresponding elemental composition and size statistics listed in Tables 3 and 4. EDS point analysis indicates that the precipitates are mainly composed of Al and N, with Al content of 25.94 %~38.40 wt.% and N content of 17.82 %~23.96 wt.%, plus minor amounts of Si, Fe and Mg, which matches the compositional feature of AlN precipitates. One measurement point (Spectrum 1) shows only 3.59% N and 1.81% O, suggesting a mixture of AlN and $Al_2O_3$. The size statistics show that the measured precipitates range from 1.058 μm to 2.436 μm, with an average size of approximately 1.5058 μm and a block-like morphology.

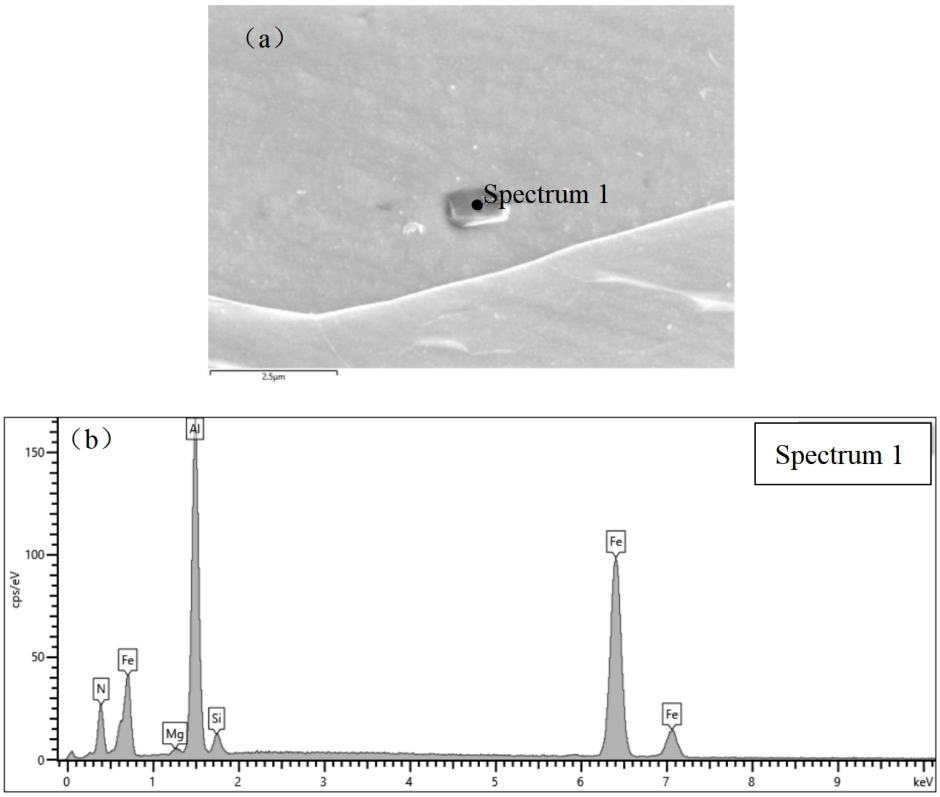


**Figure 2.** SEM and EDS spectra of the precipitate phases in non-oriented silicon steel hot-rolled sheets; (**a**) SEM; (**b**) EDS.

**Table 3.** Elemental composition of the precipitate phases in the hot-rolled sheets (wt%).

| | N | Al | Si | Fe | Mg |
|---|---|---|---|---|---|
| Spectrum 1 | 19.36 | 25.94 | 1.66 | 52.54 | 0.50 |

**Table 4.** Statistical table of precipitate phase sizes in hot-rolled steel sheets (μm).

| 1 | 2 | 3 | 4 | 5 | Average Value |
|---|---|---|---|---|---|
| 2.436 | 1.058 | 1.169 | 1.326 | 1.540 | 1.5058 |

Figure 3 shows the microstructure orientation map and micro-texture map of the normalized sheet and Table 5 lists the corresponding texture fractions. The microstructure reveals fully grown recrystallized grains. After normalizing at 875 °C, the texture is dominated by {115}<110>, {113}<361> and {112}<110>, with volume fractions of 17.1%, 16.5% and 13.0% respectively. Minor components, including {001}<350> and {001}<110>, are also present, at 11.4% and 7.83%, respectively. The maximum orientation density of the ODF map is 5.32 for the normalized condition.

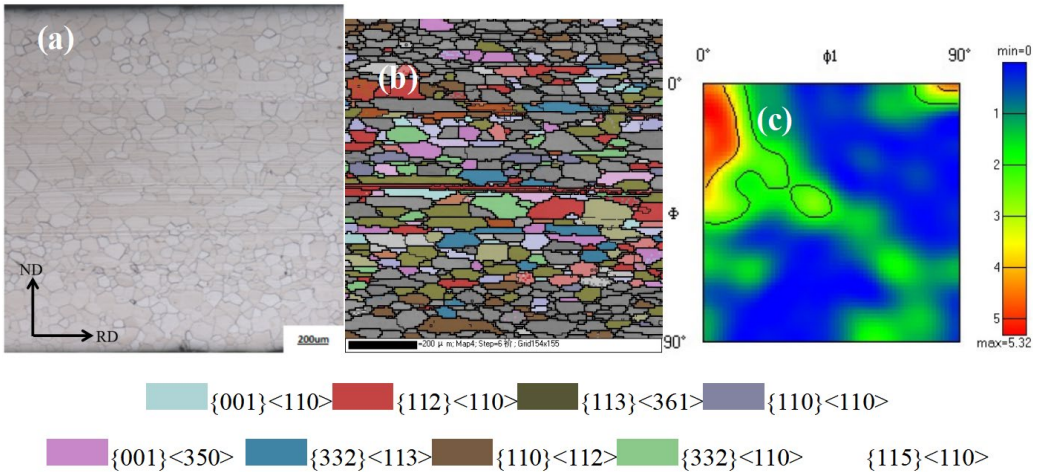


**Figure 3.** Normalized plate microstructure, orientation map and micro-texture diagram. (**a**) microstructure; (**b**) orientation map; (**c**) micro-texture diagram.

**Table 5.** Texture content of the normalized plate (%).

| {001}<110> | {110}<112> | {115}<110> | {332}<113> | {001}<350> | {112}<110> | {332}<110> | {110}<110> | {113}<361> |
|---|---|---|---|---|---|---|---|---|
| 7.83 | 5.27 | 17.1 | 4.32 | 11.4 | 13 | 4.13 | 1.72 | 16.5 |

Figure 4 shows the scanning images and energy spectra of the precipitates in the normalized plate, and Table 6 presents the corresponding elemental composition percentages of the precipitates in the normalized plate. At the same time, the size characteristics of the precipitates were statistically analyzed, with the results shown in Table 7. The elements C, N, and S are highly detrimental to the magnetic properties of non-oriented silicon steel; they form fine MnS, AlN, $Al_2O_3$, and other inclusions smaller than 0.1 μm within the steel, which significantly impede grain growth during annealing [18]. As shown in Table 5, three typical types of precipitates are mainly present in the normalized plate: the first type is MgO and $Al_2O_3$ precipitates, with the mass fractions of O, Al, Si and Mg being 2.78%, 3.91%, 2.27%, and 1.45%, respectively; the second type is AlN precipitates, with the mass fractions of Al and N being 3.37% and 1.73%, respectively, while also containing a certain amount of O and Si; the third type is MgO, CaO and CaS precipitates, with the mass fractions of O, Mg, Ca and S reaching 26.88%, 32.8%, 4.73%, and 4.22%, respectively, accompanied by small amounts of Si, C and matrix Fe. The statistical results of the precipitate

sizes in the normalized plate (Table 7) indicate that the precipitate particle sizes are 1.280 μm, 0.908 μm, and 1.542 μm, with an average particle size of approximately 1.243 μm.

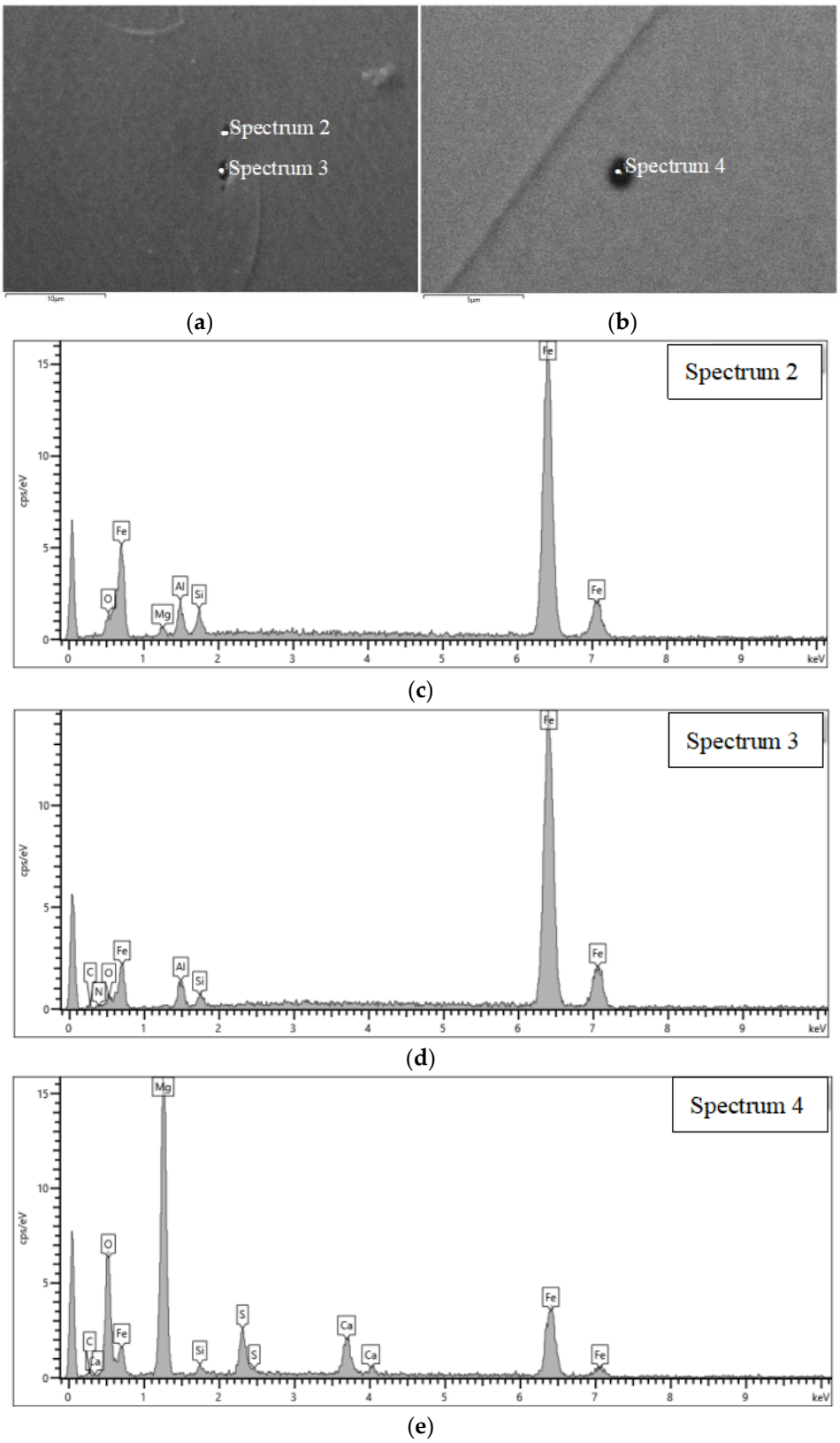


**Figure 4.** SEM and EDS of the precipitate phase in the normalized specimen. (**a**,**b**) SEM; (**c**–**e**) eds.

**Table 6.** Elemental composition of the precipitate phase in the normalized specimen (wt%).

| | O | Al | Si | Fe | Mg | C | N | S | Ca |
|---|---|---|---|---|---|---|---|---|---|
| Spectrum 2 | 2.78 | 3.91 | 2.27 | 89.58 | 1.45 | - | - | - | - |
| Spectrum 3 | 1.83 | 3.37 | 1.14 | 89.25 | - | 2.68 | 1.73 | - | - |
| Spectrum 4 | 26.88 | - | 0.84 | 26.39 | 32.8 | 4.14 | - | 4.22 | 4.73 |

**Table 7.** Statistical analysis of precipitate phase sizes in the normalized plate (μm).

| 1 | 2 | 3 | Average Value |
|---|---|---|---|
| 1.280 | 0.908 | 1.542 | 1.243 |

Figure 5 shows the cold-rolled microstructure of the 0.25 mm thick sheet. Two distinct microstructural features are observed: dark regions (marked by red boxes) containing dense shear bands inclined at an angle to the rolling direction and bright, smooth regions (marked by blue boxes) dominated by deformation bands. Shear bands are preferred sites for recrystallization nucleation during annealing, owing to their high dislocation density and stored energy [19]. Larger initial grain size before cold rolling promotes the formation of shear bands that penetrate through deformation bands and create a large orientation difference with the matrix [20]. In this work, the relatively large grain size of the normalized sheet leads to extensive shear band formation after cold rolling.

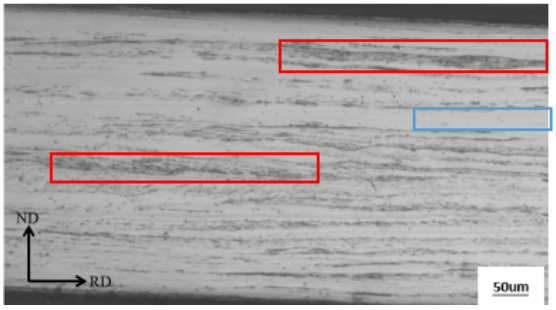


**Figure 5.** Microstructure of 0.25 mm thick cold-rolled steel sheet (The red box indicates the shear zone; the blue box indicates the deformation zone).

Figure 6 shows the metallographic microstructure of 0.25 mm thick non-oriented silicon steel after annealing at 850–1000 °C and Table 8 presents the statistical results of the average grain size of the corresponding annealed samples. From the microstructural morphology, it can be seen that the samples annealed at all temperatures have completed recrystallization. At 850 °C, the average grain size of the sample is 38.328 μm, corresponding to the fine-grained structure at the initial stage of recrystallization. When the annealing temperature increases to the range of 875–950 °C, the grains enter a stage of rapid growth, with the average grain size increasing from 70.965 μm to 141.813 μm. At 975 °C, the average grain size reaches its maximum of 161.376 μm. When the temperature rises further to 1000 °C, the average grain size decreases to 144.255 μm. This is because within the annealing temperature range of 800–1100 °C, the grains consist solely of ferrite [21], and recrystallization occurs through nucleation and growth of grains, consuming the thermally activated matrix that has undergone nucleation and recovery. During the nucleation process, there exists an incubation period, which is longer at lower annealing temperatures [22]. However, excessively high annealing temperatures can lead to abnormal grain growth, resulting in uneven grain size distribution and grain boundary pinning [13]. In summary, within the range of 850–975 °C, the annealing temperature has a significant regulatory effect on the grain size of 0.25 mm thick non-oriented silicon steel.

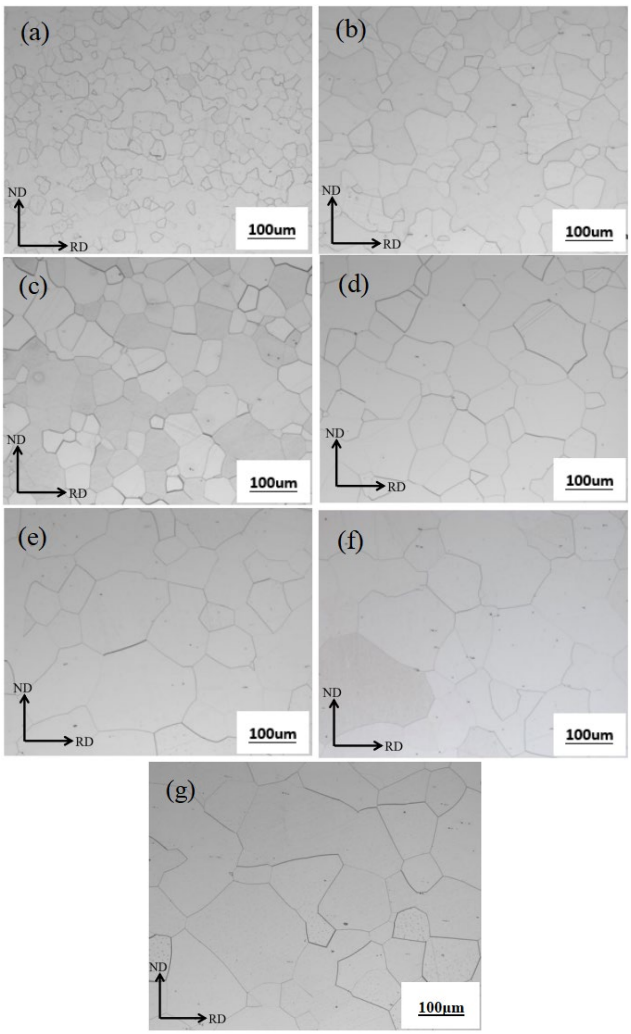


**Figure 6.** Microstructure of a 0.25 mm annealed plate. (**a**) 850 °C; (**b**) 875 °C; (**c**) 900 °C; (**d**) 925 °C; (**e**) 950 °C; (**f**) 975 °C; (**g**) 1000 °C.

**Table 8.** Grain size of 0.25 mm-thick non-oriented silicon steel at annealing temperatures of 850~1000 °C (μm).

| | **850** | **875** | **900** | **925** | **950** | **975** | **1000** |
|---|---|---|---|---|---|---|---|
| Size | 38.328 | 70.965 | 80.271 | 116.404 | 141.813 | 161.376 | 144.255 |

Figure 7 shows the orientation maps and microstructure textures of 0.25mm non-oriented silicon steel annealed at 900, 950 and 1000 °C, and Table 9 presents the corresponding texture contents of the annealed sheets. During the annealing process, recrystallization occurs, forming Goss and Cube textures [22]. After annealing at 900 °C, the texture is mainly composed of {112}<021>, {331}<013>, {114}<041> and {331}<136> orientation components, with {112}<021> being the most predominant, accounting for 21% by volume. The volume fractions of {331}<136>, {114}<041> and {331}<013> are 20.5%, 17.4% and 15.2%, respectively. When the annealing temperature rises to 950 °C, the volume fractions of the main texture components all show an increasing trend: {112}<021> increases to 27.7% and {331}<013>, {114}<041> and {331}<136> reach 23%, 20% and 22.3%, respectively. Textures such as {110}<001> and {001}<350> also exist, with Goss ({110}<001>) and {001}<350> comprising 4.6% and 3.58%, respectively. At an annealing temperature of 1000 °C, the contents of {112}<021>, {331}<013>, {114}<041>, {331}<136> and {112}<132> textures decrease to 17%, 10.4%, 11.3%, 13.3% and 10.9%, respectively, while the proportions of {110}<331>, {115}<141> and {110}<113> orientation components increase, with {110}<331>

reaching 15.4% by volume. The Goss texture content decreases to 1.12% compared with 950 °C, and a Cube texture ({001}<100>) appears with a content of 1.12%. It is generally recommended to maximize the phase fraction in the {100} and {110} textures as much as possible, particularly the {100} phase fraction, while minimizing the phase fraction in the {111} texture [18].

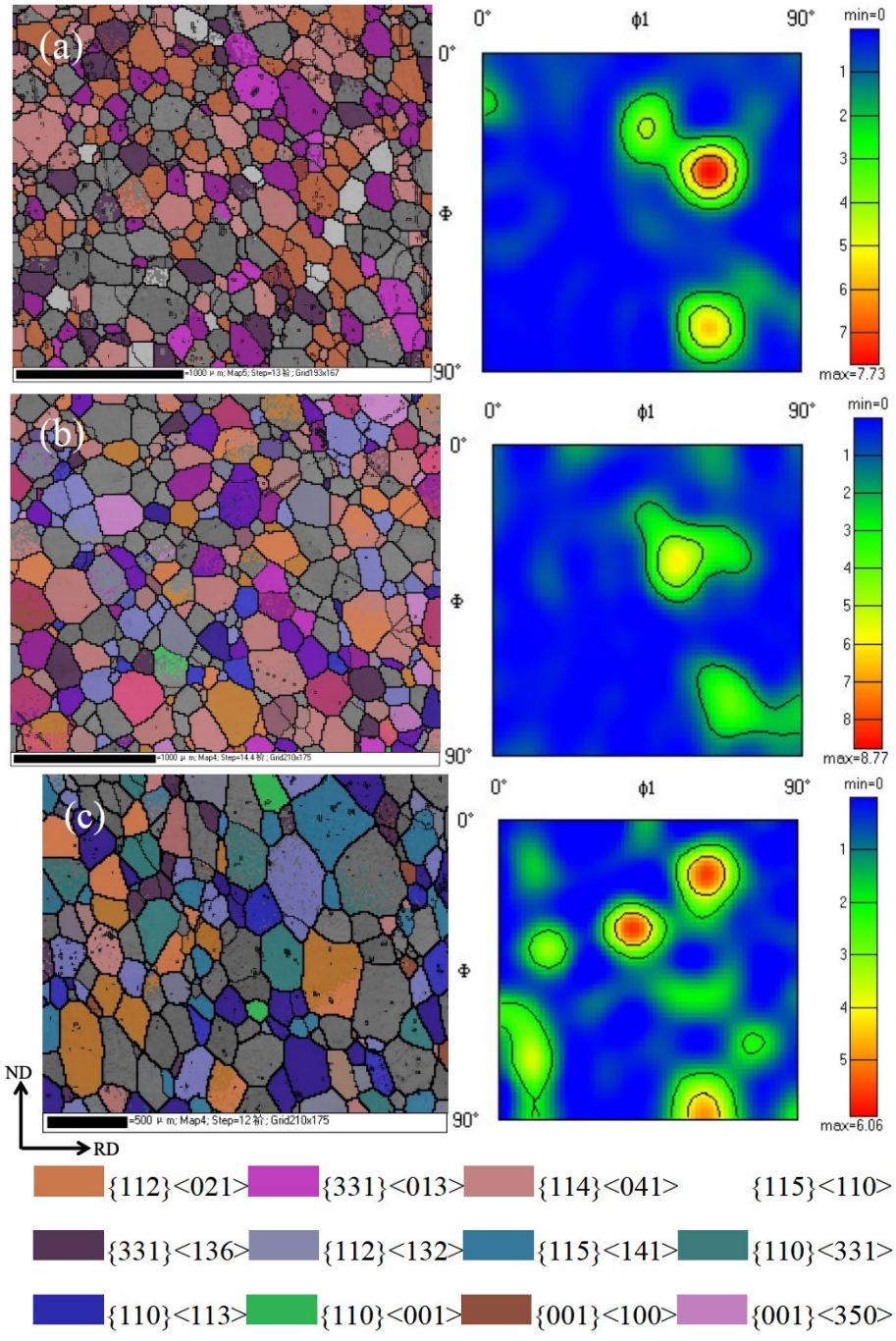


**Figure 7.** Texture maps and microstructure images of annealed sheets (**a**) 900 °C; (**b**) 950 °C; (**c**) 1000 °C.

**Table 9.** Texture content of 0.25 mm annealed sheets.

| | {112}<021> | {331}<013> | {114}<041> | {331}<136> | {115}<110> | {112}<132> | {110}<113> | {110}<001> | {001}<350> | {001}<100> | {115}<141> | {110}<331> |
|---|---|---|---|---|---|---|---|---|---|---|---|---|
| 900 °C | 21 | 15.2 | 17.4 | 20.5 | 3.89 | - | - | - | - | - | - | - |
| 950 °C | 27.7 | 23 | 20 | 22.3 | - | - | - | 4.6 | 3.58 | - | - | - |
| 1000 °C | 17 | 10.4 | 11.3 | 13.3 | - | 10.9 | 12.9 | 1.12 | - | 1.6 | 7.96 | 15.4 |

The typical precipitates in 0.25 mm non-oriented silicon steel after annealing at 900 °C were characterized morphologically and their compositions were quantitatively analyzed; the results are shown in Figure 8, and the elemental proportions and size statistics of the precipitates are listed in Tables 10 and 11, respectively. As seen in Figure 8, blocky precipitates are distributed in the matrix, with clear contours and relatively regular morphology. The results in Table 10 show that the Al, N elemental ratio is close to the stoichiometric ratio, and combined with the phase characteristics, this type of precipitate can be identified as AlN; MgO and $Al_2O_3$ precipitates are also present. The size statistics in Table 11 indicate that the diameters of the five selected precipitates range from 0.319 to 4.122 μm, with a relatively large size dispersion, and the average particle size is approximately 2.1968 μm. The pinning force of the precipitate increases as the volume fraction of the precipitate increases or as the average radius of the precipitate decreases [23]; after annealing, the radius of the precipitate increases, so the pinning force decreases following annealing.

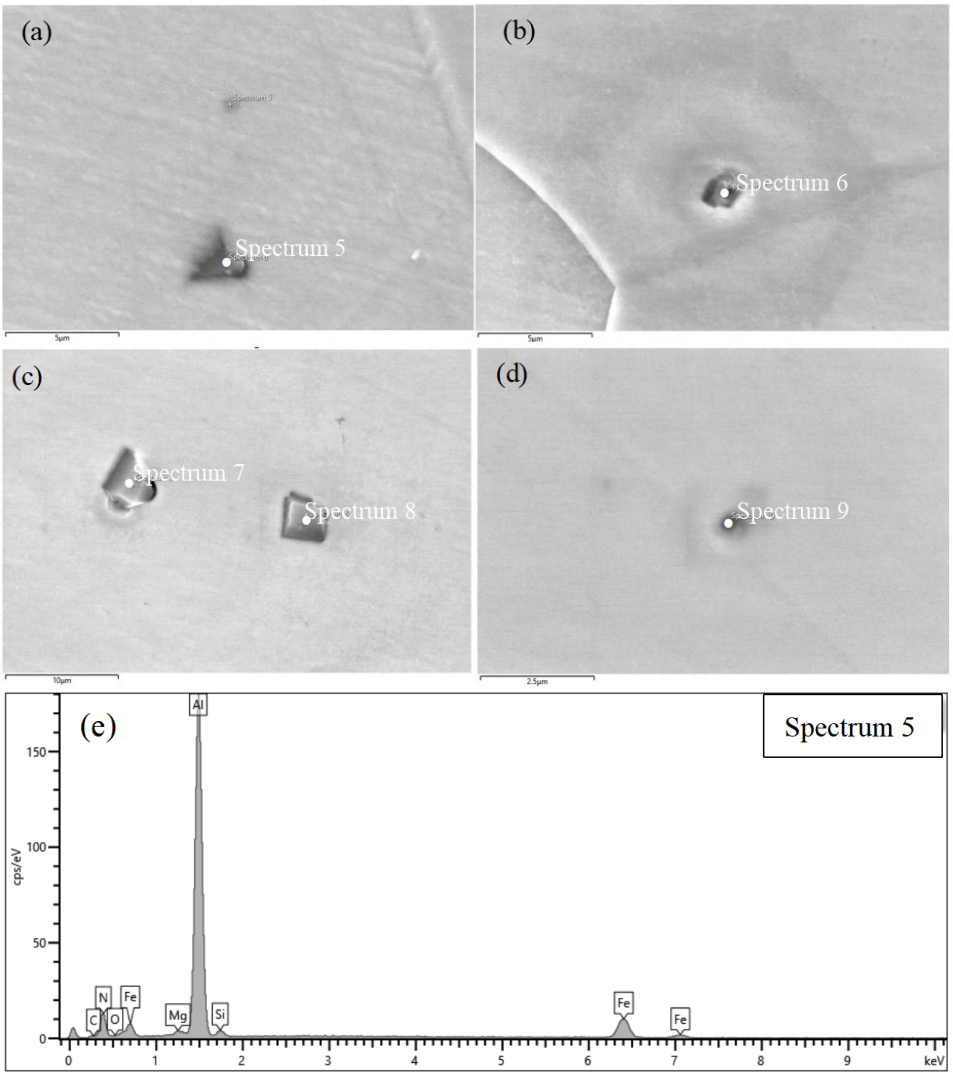

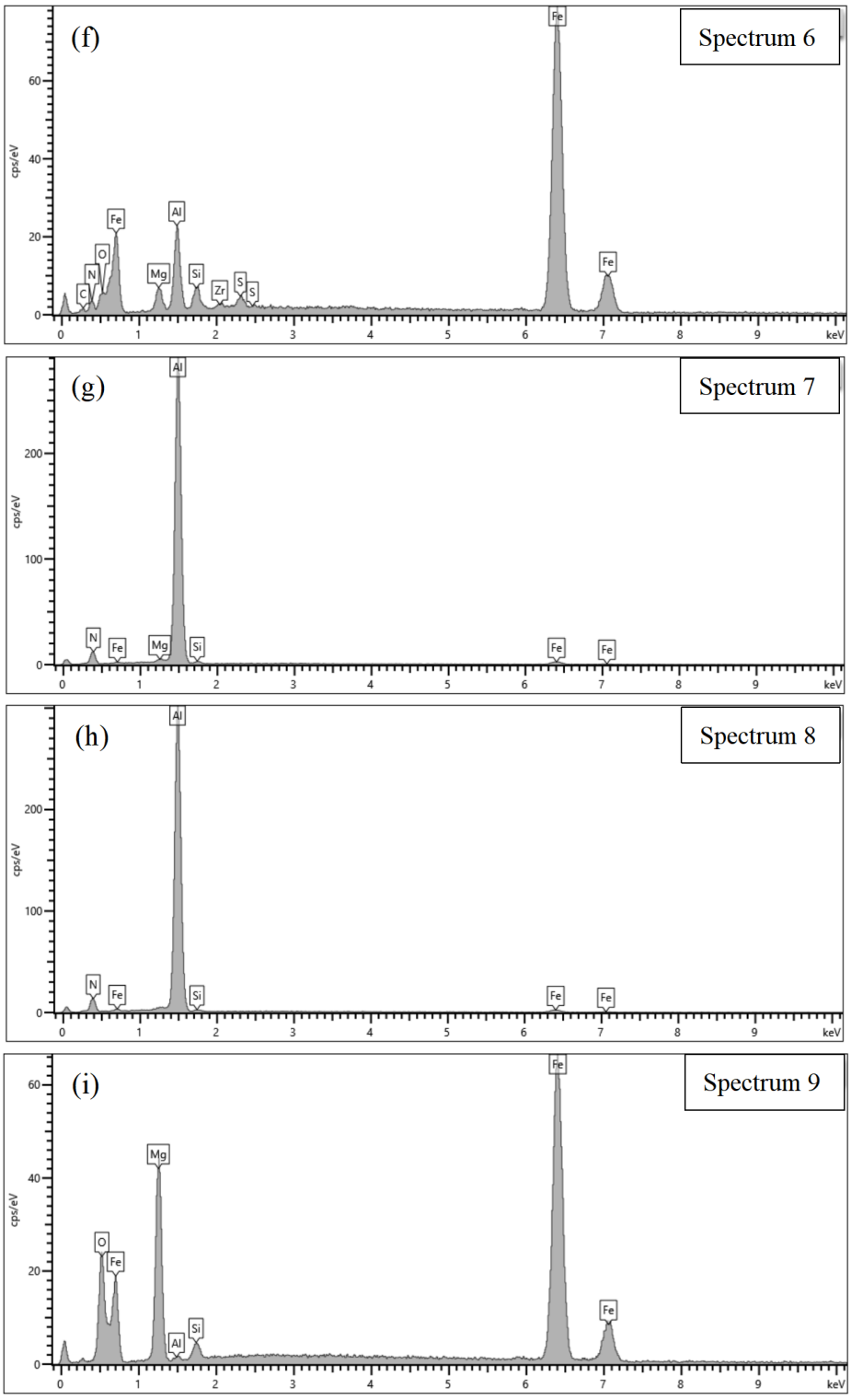


**Figure 8.** SEM and EDS of precipitate phases in annealed sheet at 900 °C. (**a**–**d**) SEM; (**e**–i) eds.

**Table 10.** Elemental composition of precipitate phases in annealed sheet at 900 °C (wt%).

| | N | Al | Si | Fe | Mg | O | S | Zr |
|---|---|---|---|---|---|---|---|---|
| Spectrum 5 | 32.74 | 49.64 | 1.41 | 14.12 | 0.56 | 1.52 | - | - |
| Spectrum 6 | 4.65 | 8.12 | 1.86 | 78.05 | 2.89 | 2.73 | 0.85 | 0.84 |
| Spectrum 7 | 31.08 | 63.64 | 0.97 | 0.19 | 0.51 | - | - | - |
| Spectrum 8 | 34.09 | 62.46 | 0.72 | 2.73 | - | - | - | - |
| Spectrum 9 | - | 0.37 | 1.22 | 67.87 | 20.15 | 10.38 | - | - |

**Table 11.** Statistical table of precipitate phase sizes in 0.25 mm annealed plates at 900 °C (μm).

| 1 | 2 | 3 | 4 | 5 | Average Value |
|---|---|---|---|---|---|
| 1.860 | 0.319 | 1.232 | 4.122 | 3.451 | 2.1968 |

Figure 9 shows the variation curves of iron loss and magnetic flux density for 0.25 mm thick non-oriented silicon steel after annealing at 850–1000 °C. The iron loss $P_{1.0/400}$ exhibits a fluctuating downward trend with increasing annealing temperature: at 850 °C, the iron loss $P_{1.0/400}$ is 12.38 W/kg, dropping to the lowest value across the entire temperature range at 875 °C, then increasing at 900 °C, gradually decreasing again after 925 °C, and reaching approximately 10.11 W/kg at 1000 °C. The magnetic flux density at 850 °C is 1.681T, which continuously increases with temperature from 875 °C to 950 °C, reaching a peak of about 1.865T at 950 °C, and then gradually decreases after 975 °C.

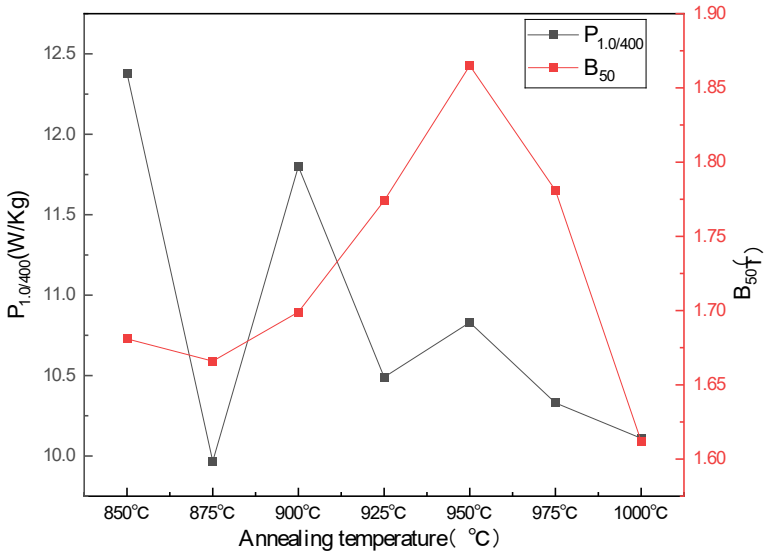


**Figure 9.** Magnetic flux density curve of 0.25 mm amorphous silicon steel.

At 900 °C annealing, the samples are mainly composed of {112}<021>, {331}<136> and other textures, with no obvious <001> favorable textures, resulting in a relatively low $B_{50}$. When the temperature is raised to 950 °C, during the recrystallization process, favorable textures containing the easily magnetized <001> axis are formed, including 4.6% {110}<001> and 3.58% {001}<350>, effectively increasing the proportion of easily magnetized directions in the rolling plane and maximizing $B_{50}$. When the annealing temperature is further increased to 1000 °C, the proportion of {110}<001> drops to 1.12% and the {001}<350> component completely disappears, greatly reducing the proportion of favorable textures, while the proportion of $\alpha$-fiber textures such as {110}<331> increases, leading to a significant decrease in B50. In summary, annealing at 950 °C enables the optimal matching of magnetic flux density and iron loss for 0.25 mm thick non-oriented silicon steel.

The hysteresis loop of $P_{1.0/400}$ after annealing at 950 °C is shown in Figure 10. The blank sample has a coercivity Hc of 62.64 A/m and a remanence Br of 515.2 mT. The smaller the area of the hysteresis loop, the fewer internal factors hinder magnetic domain pinning, making magnetization easier and resulting in relatively lower coercivity [24].

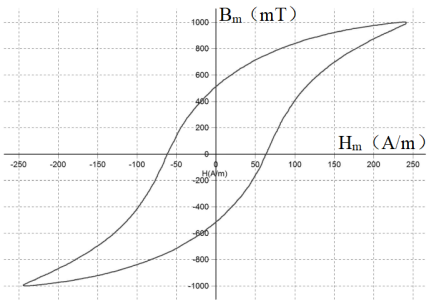


**Figure 10.** Hysteresis loop of $P_{1.0/400}$ at an annealing temperature of 950 °C.

## 4. Conclusions

(1) The annealing temperature has a significant regulatory effect on the recrystallization microstructure of 0.25 mm thick non-oriented silicon steel. Within the temperature range of 850–975 °C, as the annealing temperature increases, recrystallization progresses fully, grains grow uniformly, and the average grain size continuously increases from 38.328 μm to 161.376 μm; when the temperature rises to 1000 °C, abnormal grain growth causes mutual pinning at grain boundaries, leading to a decrease in average grain size.

(2) At an annealing temperature of 900 °C, textures such as {112}<021> and {331}<136> predominate; at 950 °C, during the nucleation and growth of recrystallization, favorable textures containing <001> easy magnetization axes, such as {110}<001> and {001}<350>, are formed, effectively enhancing in-plane magnetization capability and maximizing magnetic induction. After annealing at 1000 °C, the proportion of favorable textures decreases, the proportion of $\alpha$-fiber textures rebounds, and magnetic induction correspondingly decreases.

(3) The precipitate phase is primarily AlN, accompanied by a small amount of $Al_2O_3$, with an average grain size of 1.51 μm in the hot-rolled state; after annealing at 900 °C, the average grain size increases to 2.20 μm. Annealing at 950 °C achieves the optimal balance between magnetic induction and iron loss; $B_{50}$ is 1.865 T, iron loss $P_{1.0/400}$ is 10.85 W/kg, corresponding to a coercivity of 62.64 A/m and remanence of 515.2 mT.

(4) For this 0.25 mm ultra-thin non-oriented silicon steel, annealing temperature modulates grain size homogeneity, the competitive development of magnetization-favorable textures and AlN precipitate coarsening. The matching of proper grain geometry and a high fraction of <001> easy-axis textures is the essential structural prerequisite to realize the optimal balance between magnetic induction and high-frequency core loss.

**Author Contributions:** Conceptualization, L.F. and R.C.; methodology, X.L.; software, X.Y.; validation, X.L., L.F. and R.C.; formal analysis, L.D.; investigation, X.L.; resources, X.Y. and L.F.; data curation, L.D.; writing—original draft preparation, L.F. and R.C. All authors have read and agreed to the published version of the manuscript.

**Funding:** This research was funded by the National Natural Science Foundation of China (52361025).

**Data Availability Statement:** The original contributions presented in this study are included in the article. Further inquiries can be directed to the corresponding author.

**Conflicts of Interest:** The authors Xiaoyu Lu and Xiaoming Yuan are employed by the Inner Mongolia Baotou Steel Union Co., Ltd. The remaining authors declare that the research was conducted in the absence of any commercial or financial relationships that could be construed as a potential conflict of interest”

## References


1. Li, Y.L.; Li, J.W.; Tian, B.Z. Research and Development of High-Strength Silicon Steel Application Technology for New-Generation New Energy Vehicle Drive Motors. *Electr. Steel* **2021**, *3*, 8–12.
2. Li, Z.H.; Xie, S.K.; Wang, G.D. Dependence of recrystallization behavior and magnetic properties on grain size prior to cold rolling in high silicon non-oriented electrical steel. *J. Alloys Compd.* **2021**, *888*, 161576. https://doi.org/10.1016/j.jallcom.2021.161576.
3. Li, Z.H.; Wang, G.D.; Liu, H.T. Effects of processing routes on recrystallization texture development and magnetic properties of 0.10 mm ultrathin non-oriented electrical steel sheets for high-frequency application. *J. Alloys Compd.* **2022**, *16*, 79–84. https://doi.org/10.1016/j.jallcom.2022.167984.
4. Fan, L.F.; Zhu, Y.; Yue, E. Microstructure and texture evolution of ultra-thin high grade non-oriented silicon steel used in new energy vehicle. *Mater. Res. Express* **2022**, *9*, 096515. https://doi.org/10.1088/2053-1591/ac9119.
5. Fang, F.; Che, S.; Wang, F. Microstructure evolution and strengthening mechanism in thin-gauge non-oriented silicon steel with high strength. *J. Magn. Magn. Mater.* **2022**, *16*, 91–97. https://doi.org/10.1016/j.jmmm.2022.169791.
6. Rong, Y.; Wang, G.; Kong, Q. Study on the influence of ultra-thin non-oriented silicon steel sheet on the performance of ultra-high-speed permanent magnet motor. *AIP Adv.* **2022**, *12*, 065307. https://doi.org/10.1063/5.0090234.
7. Li, Z.H.; Xie, S.K.; Wang, G.D. Ultrathin-gauge high silicon non-oriented electrical steel with high permeability and low core loss fabricated by optimized two-stage cold rolling method. *Mater. Charact.* **2021**, *183*, 1–17. https://doi.org/10.1016/j.matchar.2021.111593.
8. Tu, Y.; Meng, L.; Zhang, N. Evolutions of Cube (001) and 115 Orientations in Cold-Rolled Ultra-Thin Non-Oriented Silicon Steel. *Materials* **2023**, *16*, 6735. https://doi.org/10.3390/ma16206735.
9. Huang, X.L.; Wang, Y.P.; Liu, H.T. Effects of normalizing and annealing temperatures on microstructure, texture evolution, and magnetic properties of thin-section high-silicon non-oriented silicon steel. *Electr. Power Steel* **2025**, *7*, 25–32.
10. Li, X.; Luo, W.; Dai, Z.Y. Effect of annealing temperature on microstructure, texture, and properties of high-strength non-oriented silicon steel. *Electr. Power Steel* **2025**, *7*, 1–6.
11. Yin, P.; Niu, Y.H.; Shao, K.X.; Qiao, J.L.; Wang, H.J. Effects of annealing temperature and time on the microstructure and texture of W350 high-grade non-oriented silicon steel. *J. Mater. Heat Treat.* **2025**, *46*, 112–121.
12. Yu, L.; Luo, H.W. Effects of Partial Recrystallization Annealing on the Magnetic and Mechanical Properties of Non-Directionally Coated Silicon Steel. *Acta Metall. Sin.* **2020**, *56*, 291–300.
13. Jiao, H.; Wu, W.; Hou, Z. Ultrastrong 100 texture in twin-roll strip cast non-oriented electrical steel through two-step annealing. *Scr. Mater.* **2024**, *243*, 115998. https://doi.org/10.1016/j.scriptamat.2024.115998.
14. Liao, T.P.; Zhang, L.X.; Wu, Y.X. Effects of cold rolling reduction on microstructure and texture of non-oriented silicon steel for drive motors. *Nonferrous Met. Sci. Eng.***2024,** 14, 1–9.
15. Chen, M.X.; Shi, L.F.; Xia, X.L. Effect of cold rolling reduction on microstructure and texture of 3.3%Si non-oriented silicon steel. *Electr. Power Steel* **2026**, *8*, 19–26.
16. Xiao, L.J.; Lei, W.; Fan, L.F. Effect of preparation process on microstructure and texture of 0.65 mm non-oriented silicon steel with 2%Si critical grade. *J. Mater. Sci. Technol.* **2026**,*40*,1–20.
17. Jiang, P.; Bai, X.L.; Niu, Y.H. Effects of constant temperature and time on the microstructure and texture of 2.98% Si non-oriented silicon steel. *Electr. Steel* **2023**, *5*, 25–31.
18. Liu, P.C.; Wu, Y.X.; Liu, B.Z.; Wu, Z.W.; Sun, T.T. Comprehensive process-based microstructure-property analysis of rare-earth-doped non-oriented silicon steel 50W470. *Baogang Technol.* **2025**, *51*, 27–32+48.
19. Jin, Z.L.; Ren, H.P.; Wang, Y.F. Evolution of cold-rolling and annealing textures in non-oriented electrical steel. *Steel* **2007**, 63–66. https://doi.org/10.1029/2026JD046812.
20. Fang, F.; Wang, J.; Yang, J. Formation of η-oriented shear bands and its significant impact on recrystallization texture in strip-cast electrical steel. *J. Mater. Res. Technol.* **2022**, *21*, 1770–1783. https://doi.org/10.1016/j.jmrt.2022.10.034.
21. Ohnuma, I.; Abe, S.; Shimenouchi, S. Experimental and Thermodynamic Studies of the Fe–Si Binary System. *ISIJ Int.* **2012**, *52*, 540–548. https://doi.org/10.2355/isijinternational.52.540.
22. Wang, H.J.; Niu, Y.H.; Qiao, J.L. Effect of annealing process on grain size and texture strength of non-oriented silicon steel. *Met. Heat Treat.* **2023**, *48*, 44–55.

23. Wang, Y.; Zhu, C.Y.; Li, G.Q.; Liu, Y.; Zhou, B.W. The effect of Nb content on precipitates, microstructure and texture of grain oriented silicon steel. *High Temp. Mater. Processes* **2019**, *38*, 628–638.
24. Li, S.; Zu, G.; Jiang, X. Microstructure and Magnetic Properties of Fe-4.5% Si Thin-Gauge Non-Oriented Electrical Steel. *Met. Mater. Int.* **2024**, *31*, 613–622. https://doi.org/10.1007/s12540-024-01758-x.

**Disclaimer/Publisher's Note:** The statements, opinions and data contained in all publications are solely those of the individual author(s) and contributor(s) and not of MDPI and/or the editor(s). MDPI and/or the editor(s) disclaim responsibility for any injury to people or property resulting from any ideas, methods, instructions or products referred to in the content.